Catalysis Science & Technology

Role of polyoxometalate precursors and supports in the selective oxidation of methane into formaldehyde using supported metal oxide subnanocluster catalysts

Journal:	*Catalysis Science & Technology*
Manuscript ID	CY-ART-05-2023-000750.R1
Article Type:	Paper
Date Submitted by the Author:	26-Jun-2023
Complete List of Authors:	Wachi, Keiju; The University of Tokyo, Department of Applied Chemistry, School of Engineering, Yabe, Tomohiro; The University of Tokyo, Applied Chemistry Suzuki, Takaaki; The University of Tokyo, Department of Applied Chemistry, School of Engineering, Yonesato, Kentaro; The University of Tokyo, Department of Applied Chemistry, School of Engineering, Suzuki, Kosuke; The University of Tokyo, Department of Applied Chemistry, School of Engineering, Yamaguchi, Kazuya; The University of Tokyo, Applied Chemistry

ARTICLE

Role of polyoxometalate precursors and supports in the selective oxidation of methane into formaldehyde using supported metal oxide subnanocluster catalysts

Received 00th January 20xx,
Accepted 00th January 20xx

DOI: 10.1039/x0xx00000x

Keiju Wachi, Tomohiro Yabe*, Takaaki Suzuki, Kentaro Yonesato, Kosuke Suzuki, and Kazuya Yamaguchi*

The direct synthesis of useful chemicals from methane (CH_4) is desirable; however, the products are prone to nonselective overoxidation, leading to the formation of CO_2. A previous study developed a supported iron oxide subnanocluster catalyst with high thermal stability using iron-containing polyoxometalates (POMs) as precursors to selectively produce formaldehyde (HCHO) and CO. Herein, we investigated various supported POM-based catalysts to further improve the selectivity to HCHO via CH_4 oxidation, specifically by suppressing the pyrolysis and overoxidation of HCHO. After examining various metal-containing POM precursors and supports, we found that catalysts prepared using mononuclear- and dinuclear-iron-containing POM precursors supported on SiO_2 with a high specific surface area were effective and yielded relatively high quantities of HCHO. *In situ* diffuse reflectance infrared Fourier transform spectroscopy (DRIFTS) measurements under HCHO flow demonstrated that the pyrolysis and oxidation of HCHO were suppressed on SiO_2, while the pyrolysis of HCHO was promoted on Al_2O_3. Furthermore, *in situ* DRIFTS measurements conducted at different temperatures revealed that HCHO was not decomposed or oxidized at 500 °C in the absence of catalysts.

Introduction

Methane (CH_4), the main component of natural gas, is abundantly available worldwide, including in unconventional resources, such as biogas (including bio-methanation gas)[1–3] and CH_4 hydrates.[4] Furthermore, the production of carbon-neutral CH_4, such as in power-to-gas technology, is expected to increase in the future. This production involves synthesizing CH_4 via methanation processes that utilize green hydrogen produced from renewable energy sources, such as water electrolysis and CO_2 emitted from power plants and factories.[5–7] Thus, CH_4 is gaining attention as a major energy resource and a promising chemical raw material.[8–11] However, CH_4, with its tetrahedral shape and four identical C–H bonds, has the highest C–H bond energy (439 kJ mol^{-1}) among sp^3-hybridized hydrocarbons and is known as the least reactive alkane, making it very challenging to chemically convert into useful compounds.[12]

There are two methods for CH_4 conversion: indirect conversion via synthesis gas (syngas) and direct conversion to useful compounds, such as formaldehyde (HCHO), in one step.[13] Indirect conversion involves a syngas process, which is a high-temperature and high-pressure process that requires complicated and expensive equipment and significant energy consumption. Therefore, an economically viable direct conversion process of CH_4 into high-value-added chemicals is desired. One approach to economically achieve direct CH_4 conversion is to selectively oxidize CH_4 to oxygenates using O_2. However, the target products are susceptible to thermal decomposition or sequential oxidation under the harsh oxidation conditions required for CH_4 activation. Therefore, developing a catalytic process that selectively synthesizes the desired products while suppressing sequential reactions is an urgent challenge for ensuring the stable supply of CH_4 oxidation-derived chemicals.

Catalysts for synthesizing HCHO from CH_4 have been developed since the 1980s, and various types of catalyst systems have been proposed, such as oxide catalysts,[14,15] supported catalysts,[16–19] and zeolite catalysts.[20,21] Commonly investigated oxide catalysts include molybdenum,[16,17,19,22] vanadium,[16,23] iron,[24] copper,[22,25] cobalt,[21] and tungsten.[14,26] However, bulk oxide and large nanoparticle catalysts have demonstrated relatively low selectivity to HCHO. For example, large nanoparticles of VO_x on the VO_x/Al_2O_3 catalyst reduced both CH_4 conversion and HCHO selectivity in CH_4 oxidation.[23] Additionally, Zhang *et al.* reported that in molybdenum oxide catalysts, CH_4 conversion and HCHO selectivity were related to the density of Mo=O bonds; namely, Mo=O bonds on $Zr(MoO_4)_2$ were responsible for HCHO production, whereas excess lattice oxygen and bulk MoO_3 caused overoxidation of HCHO.[27] In the case of iron oxide catalysts, isolated active lattice oxygen atoms on the surface of iron oxides helped to suppress overoxidation during CH_4 oxidation.[28] Thus, supported metal oxide

Department of Applied Chemistry, School of Engineering, The University of Tokyo, 7-3-1 Hongo, Bunkyo-ku, Tokyo 113-8656, Japan. E-mail: kyama@appchem.t.u-tokyo.ac.jp, tyabe@g.ecc.u-tokyo.ac.jp

†Electronic Supplementary Information (ESI) available: See DOI: 10.1039/x0xx00000x

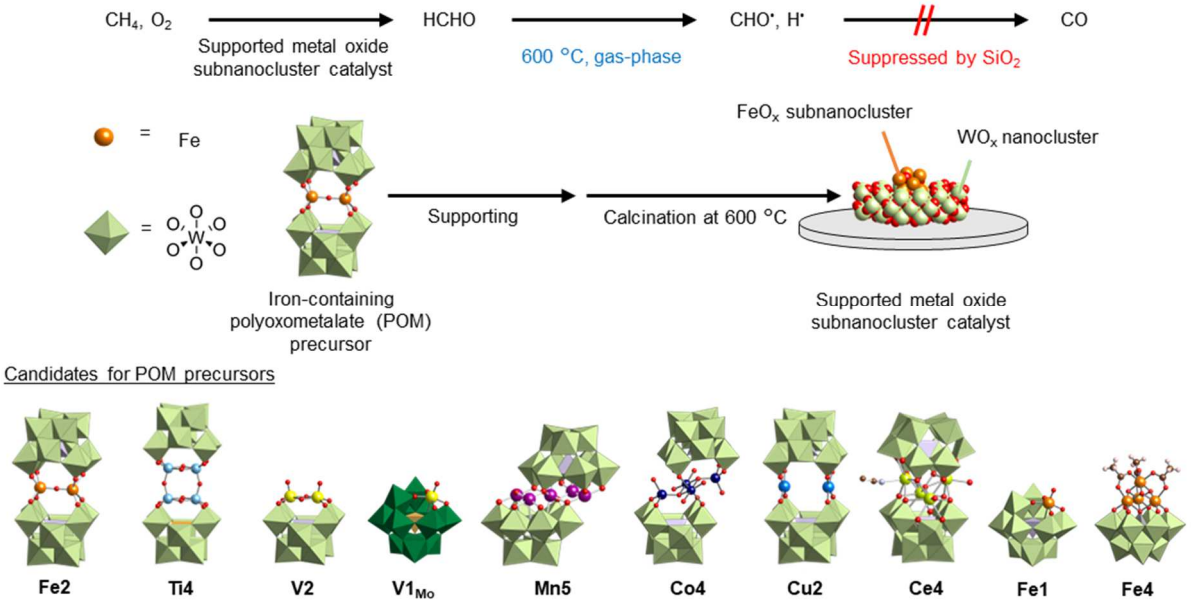

Fig. 1 Schematic diagram of the catalytic performance for CH_4 oxidation using supported metal oxide subnanocluster catalyst prepared from polyoxometalates.

nanocluster catalysts have attracted attention, with reported examples including supported CuO_x,[29] FeO_x,[30,31] MoO_x,[32] and VO_x nanocluster catalysts.[33]

The choice of catalyst supports is also significant in selective CH_4 oxidation, and various oxide supports have been investigated, with SiO_2 being recognized as the most suitable support. Kobayashi *et al.* discovered that highly dispersed Fe^{3+} species on SiO_2 with isolated tetrahedrally coordinated Fe–O species significantly promoted selective HCHO production.[34] Although detailed mechanistic studies are still in progress, it is evident that highly dispersed active sites in FeO_x nanoclusters on SiO_2 are essential for achieving selective HCHO production. Similarly, there is ongoing debate regarding the reaction mechanism of pyrolysis and overoxidation on SiO_2 and other supports.

A polyoxometalate (POM) is an anionic metal oxide cluster consisting of metal–oxygen polyhedral units, such as $\{WO_6\}$.[35,36] The structure formed by eliminating some of the polyhedral units is called a lacunary POM, which functions as an inorganic multidentate ligand and allows the incorporation of different metals.[37–39] Recent studies have reported a new synthesis method for introducing various multinuclear metal oxide clusters into lacunary POMs in organic solvents.[40–44] Furthermore, a previous study used a diiron-containing POM (**Fe2**) as a precursor to in situ form FeO_x subnanoclusters on SiO_2, which served as the active species to selectively converted CH_4 into HCHO and CO.[45] This catalyst maintained the catalytic activity at 600 °C for 72 h, because the FeO_x subnanoclusters were dispersed in tungsten oxide species and inhibited from aggregation and deactivation. Another study successfully developed a method to achieve highly dispersed POM tetra-*n*-butylammonium (TBA) salts on various supports.[46] Therefore, using POMs with different multinuclear metal oxide cores as catalyst precursors allows the investigation of various highly stable metal oxide subnanoclusters for the selective conversion of CH_4 to HCHO.

In this study, to further enhance the HCHO yield, we investigated CH_4 oxidation by using various POMs supported on SiO_2 as catalyst precursors (Fig. 1). Catalysts prepared using mononuclear (**Fe1**)- and dinuclear (**Fe2**)-iron-containing POM precursors supported on SiO_2 produced relatively high yields of HCHO. Furthermore, we investigated CH_4 oxidation using various supports. The results demonstrated that although CH_4 conversion increased when using **Fe2**/Al_2O_3 and **Fe2**/CeO_2, overoxidation to CO_2 was promoted. We observed that catalysts prepared using SiO_2 (i.e., **Fe2**/SiO_2) exhibited significantly higher HCHO yields than catalysts prepared using other supports. In addition, to elucidate the mechanism underlying the suppression of overoxidation of HCHO on **Fe2**/SiO_2, we investigated HCHO oxidation using Al_2O_3 and SiO_2 with different specific surface areas. We found that SiO_2 suppressed HCHO pyrolysis, and the suppression was enhanced as the specific surface area of SiO_2 increased. Moreover, we conducted temperature variation tests on HCHO oxidation and observed that HCHO was minimally decomposed or oxidized at 500 °C in the absence of catalysts.

Experimental

Catalyst characterization

Cold-spray ionization (CSI)-mass spectra were recorded on a JEOL JMS-T100CS spectrometer. Infrared (IR) spectra were measured on a JASCO FT/IR-4100 spectrophotometer using KBr disks. Inductively coupled plasma atomic emission spectroscopy (ICP-AES) analysis was performed on a Shimadzu ICPS-8100 instrument. Brunauer–Emmett–Teller (BET) surface areas were measured by N_2 adsorption at −196 °C using a Micromeritics TriStar II Plus instrument. Raman spectra were recorded on a

JASCO NRS-5100 spectrometer. The measurement conditions included an irradiation laser wavelength of 532 nm and a laser power of 10.2 mW, and the data were collected twice with a measurement time of 3 min. X-ray absorption spectroscopy (XAS) of the Fe K-edge was performed using the transmission and fluorescence method at the BL14B2 beamline of SPring-8 (proposal numbers 2022B1656 and 2023A1512). The X-ray beam was monochromatized using a Si (111) monochromator, and the energy was calibrated using an Fe metal foil for the Fe K-edge XAS. X-ray absorption near-edge structure (XANES) and extended X-ray absorption fine structure (EXAFS) data were analyzed using Athena and Artemis software (Demeter, version 0.9.26; Bruce Ravel). The k^3-weighted EXAFS spectra were Fourier-transformed into *R*-space in the range of 3–12 $Å^{-1}$ for Fe. The XAS measurement methods and EXAFS analyses are explained in detail in the electronic supplementary information (ESI).

Reagents

Dichloromethane, diethyl ether, and acetonitrile were purchased from Kanto Chemicals. SiO_2 (CARiACT Q-6, Q-10, Q-30, or Q-50, Fuji Silysia Chemical Ltd.), Al_2O_3 (KHS-46, Sumitomo Chemical Co. Ltd.), ZrO_2 (JRC-ZRO-6, Daiichi Kigenso Kagaku Kogyo Co., Ltd), CeO_2 (JRC-CEO-5, Daiichi Kigenso Kagaku Kogyo Co., Ltd.), TiO_2 (ST-01, ISHIHARA SANGYO KAISHA, Ltd), Nb_2O_5 (JRC-NBO-1, Companhia Brasileira de Metalurgia e Mineração), hydroxyapatite (HAP, Cat. No. 012-14882 FUJIFILM Wako Pure Chemical Corporation), and boron nitride (BN, Cat. No. 028-02281, FUJIFILM Wako Pure Chemical Corporation) were acquired from commercial sources. To represent SiO_2 with different specific surface areas, CARiACT Q-6, CARiACT Q-30, and CARiACT Q-50 are denoted as SiO_2-Q6, SiO_2-Q30, and SiO_2-Q50, respectively. SiO_2 without any specific indication refers to CARiACT Q-10. $Fe_3O(CH_3CO_2)_7(H_2O)_3$[47] and $TBA_4[SiW_9O_{28}(OCH_3)_6]$ (**SiW9-OMe**)[48,49] were synthesized according to the reported procedures.

Synthesis of various POMs

$TBA_8H_4Fe_2O(SiW_{10}O_{36})_2$ (**Fe2**),[45] $TBA_6Ti_4O_2(OH)_4(PW_{10}O_{36})_2$ (**Ti4**),[50] $TBA_4V_2O_2(OH)_2SiW_{10}O_{36}$ (**V2**),[51] $TBA_4VOPMo_{11}O_{39}$ (**$V1_{Mo}$**),[52] $TBA_7HMn_5(OH)_2(SiW_9O_{34})_2$ (**Mn5**),[42] $TBA_8H_4Co_4(OH)_4(SiW_{10}O_{36})_2$ (**Co4**),[53] $TBA_8H_4Cu_2(SiW_{10}O_{36})_2$ (**Cu2**),[40] $TBA_6Ce_4(H_2O)_2(CH_3CN)_2O(SiW_{10}O_{36})_2$ (**Ce4**),[41] and $TBA_4HFe(H_2O)SiW_{11}O_{39}$ (**Fe1**)[54,55] were synthesized according to the reported procedures. In addition, $TBA_4Fe_4(OH)_3(CH_3CO_2)_3SiW_9O_{34}$ (**Fe4**) was synthesized according to the following procedure. **SiW9-OMe** (500 mg, 152 μmol) was added to a dichloromethane solution (40 mL) of $Fe_3O(CH_3CO_2)_7(H_2O)_3$ (134 mg, 205 μmol), and the resulting solution was stirred for 24 h at room temperature. Then, the remaining precipitate was filtered off, and the filtrate was dropped into diethyl ether (40 mL). Finally, the generated precipitate was collected by filtration through a membrane filter. After vacuum drying, a powder sample of **Fe4** was obtained. The anionic structure of **Fe4** was estimated from the IR spectra (Fig. S1), ICP-AES elemental analysis, and CSI-mass spectrum (Fig. S2), as described below. The IR spectra illustrated acetate peaks slightly shifted from those of $Fe_3O(CH_3CO_2)_7(H_2O)_3$. The elemental analysis confirmed that four Fe^{3+} ions were introduced into an $[SiW_9O_{34}]^{10-}$ (**SiW9**) unit. The CSI-mass spectrum indicated the presence of a molecule containing four iron atoms, an **SiW9** unit, three hydroxide ligands, and three acetate ligands (Fig. S2). These results suggested that **Fe4** had a cubane-type structure, as illustrated in Fig. 1, since a similar structure was reported for a manganese analogue according to the IR results.[56] IR (KBr pellet, cm^{-1}): 3441, 2962, 2874, 1631, 1581, 1544, 1485, 1460, 1382, 1275, 1152, 1106, 1000, 958, 909, 804, 672, 524, 376, 359, 324, 319, 303, 297, 290, 282, 278, 271, 257, 252. Elemental analysis: calcd (%) for $TBA_4Fe_4(OH)_3(CH_3CO_2)_3SiW_9O_{34}\cdot 2CH_2Cl_2$, Si 0.74, Fe 5.85, W 43.33; found Si 0.74, Fe, 5.87, W 43.38. Positive-ion CSI-mass (acetonitrile): m/z = 3891.36, $[TBA_5Fe_4(OH)_3(CH_3CO_2)_3SiW_9O_{34}]^+$ (theoretical m/z = 3890.48).

Preparation of POM-supported catalysts

Various types of POMs were generally dispersed on supports with the loading amount of 10 wt% using the incipient wetness method.[46] The preparation method of **Fe2**/SiO_2 is described as a typical example. A TBA salt of **Fe2** (100 mg) was dissolved in acetonitrile (2 mL). Then, the resulting solution was dropped onto a thin layer of SiO_2 (900 mg) spread on an evaporation tray. The resulting powder was dried at 100 °C for 5 h and then calcined at 600 °C for 5 h under air atmosphere, giving the **Fe2**/SiO_2 catalyst. Various kinds of supported catalysts were prepared by the same method using POM precursors shown in Fig. 1. These supported catalysts were denoted using the abbreviation of the POM precursors and supports, such as **Fe1**/SiO2, **Fe2**/SiO_2, and **Fe4**/SiO_2. As for **Fe2**/SiO_2, the catalyst with 35 wt% **Fe2** (35**Fe2**/SiO_2) was also prepared to align the loading amount of iron with **Fe4**/SiO_2. Additionally, Cs-**Fe2**/SiO_2 was prepared following our previous report.[46] Briefly, TBA-**Fe2** was supported on SiO_2 in acetonitrile using the incipient wetness method. Then, Cs-**Fe2**/SiO_2 was obtained by cation exchange from TBA-**Fe2**/SiO_2 using cesium trifluoromethanesulfonate as the Cs source in ethanol.

Evaluation of CH_4 and HCHO oxidation performance

Catalytic performance tests for CH_4 oxidation were conducted using a fixed-bed flow-type reactor schematically illustrated in Fig. S3a. After 100 mg of catalyst was loaded into a quartz tube reactor (6.0 mm i.d.), the reactant gas (CH_4:O_2:Ar = 2:1:7, total flow rate: 50 mL min^{-1}) was introduced into the reactor. Then, the input temperature of the tube furnace containing the catalyst was increased to 600 °C at a rate of 10 °C min^{-1}. The inlet and outlet gases were heated to 100 °C to reduce the temperature variation in the catalyst bed and to suppress the condensation of products. When the furnace temperature reached 600 °C, it was maintained for 1 h to allow the activity to stabilize. Then, HCHO was trapped in 20 mL of an aqueous solution containing 2 g of Na_2SO_3 and 50 μL of H_2SO_4, and the amount of trapped HCHO was determined by titration with an aqueous solution of NaOH (0.1 M). CO and CO_2 were analyzed

immediately before and after HCHO collection using a Nexis GC-2030 gas chromatograph equipped with a barrier discharge ionization detector (Shimadzu Corporation) and a Shincarbon-ST packed column. The respective calculation formulas for CH_4 conversion, product selectivity, and product yield in this study are as follows:

$$CH_4 \text{ conv. (\%)} = \frac{\text{Total carbon moles of HCHO, CO, and } CO_2}{\text{A carbon mole of input } CH_4} \times 100$$

$$\text{Product sel. (\%)} = \frac{\text{A carbon mole of HCHO, CO, or } CO_2}{\text{Total carbon moles of HCHO, CO, and } CO_2} \times 100$$

$$\text{Product yield (\%)} = CH_4 \text{ conv. (\%)} \times \text{Product sel. (\%)} \div 100$$

In the pyrolysis and oxidation test of HCHO, gaseous HCHO was generated by flowing Ar or O_2/Ar gas through 10 g of paraformaldehyde heated to 55 °C, as illustrated in Fig. S3b.

In situ DRIFTS measurement

Diffuse reflectance infrared Fourier transform spectroscopy (DRIFTS) was performed using a JASCO FT/IR-6700 spectrometer equipped with an *in situ* sample cell in the range of 1500–4000 cm^{-1} at a resolution of 4 cm^{-1} (number of scans: 64). The samples were loaded onto a sample plate (6 mm diameter) and placed on the heater in the IR cell. The sample was pretreated by heating in a vacuum at 600 °C for 1 h, and the background spectrum was measured. After the pretreatment, the sample was exposed to approximately 1% HCHO in N_2 (20 mL min^{-1}) for 1 h. Then, the cell was evacuated into a vacuum at 600 °C, and the DRIFTS spectra were measured both in the reactant gas and in a vacuum. HCHO was generated in the same manner as described above.

Results and discussion

CH_4 oxidation using various catalysts

First, the catalytic performance for CH_4 oxidation was investigated for various POM-based catalysts at 600 °C under atmospheric pressure, and the results are presented in Table 1. **Ti4**/SiO_2, **V2**/SiO_2, **$V1_{Mo}$**/SiO_2, **Cu2**/SiO_2, and **Ce4**/SiO_2 exhibited relatively low CH_4 conversion (Table 1, Entries 2–4, 7, and 8). Although there have been several reports[16,17,19,22,23,25] on the oxidation of CH_4 to HCHO using vanadium, molybdenum, and copper oxides, the CH_4 oxidation performance using these POM precursors supported on SiO_2 was much lower than that using **Fe2**/SiO_2 (Table 1, Entry 1). Particularly, the use of **Ce4**/SiO_2 resulted in minimal HCHO formation, with significant CO_2 formation from complete CH_4 oxidation (Table 1, Entry 8). In contrast, although **Fe2**/SiO_2, **Mn5**/SiO_2, and **Co4**/SiO_2 exhibited relatively high CH_4 conversion, the overoxidation to CO_x (CO and CO_2) was more pronounced for **Mn5**/SiO_2 and **Co4**/SiO_2 than for **Fe2**/SiO_2 (Table 1, Entries 1, 5, and 6). In the case of iron, reducing the cluster size promoted the partial oxidation of CH_4 to HCHO, while the catalytic performance of manganese and cobalt nanoclusters remained similar to that of bulk oxides[57] or nanoparticles.[58] Thus, the catalytic performance for CH_4 oxidation on SiO_2-supported metal oxide subnanocluster catalysts prepared from various POM precursors indicated that **Fe2**/SiO_2 catalysts exhibited the highest HCHO yield among the metal oxide subnanocluster catalysts with 3d metal or Ce metal multinuclear structures.

Table 1 Catalytic performance in CH_4 oxidation for various catalysts prepared from POM precursors[a]

Entry	Catalyst	Conv. [%]	Sel. [%]			Yield [%]
		CH_4	HCHO	CO	CO_2	HCHO
1	**Fe2**/SiO_2	1.4	41	45	14	0.57
2	**Ti4**/SiO_2	0.40	82	5	13	0.33
3	**V2**/SiO_2	0.44	55	27	18	0.24
4	**$V1_{Mo}$**/SiO_2	0.52	63	22	15	0.33
5	**Mn5**/SiO_2	0.97	25	45	30	0.24
6	**Co4**/SiO_2	1.4	22	52	26	0.30
7	**Cu2**/SiO_2	0.69	47	27	26	0.33
8	**Ce4**/SiO_2	0.56	–	66	34	–
9	**Fe1**/SiO_2	1.4	54	32	13	0.73
10	**Fe4**/SiO_2	3.0	11	62	28	0.33
11	35**Fe2**/SiO_2	1.9	29	58	13	0.55
12	Cs-**Fe2**/SiO_2	0.67	73	20	7	0.49

[a]Reaction conditions: 10 wt% supported catalyst (100 mg), CH_4:O_2:Ar = 2:1:7, 50 mL min^{-1}, 1 atm, 600 °C.

Next, the catalytic performance for CH_4 oxidation was investigated for various Fe-POM-based catalysts prepared using iron-containing POM precursors with various multinuclear oxide cores at 600 °C under atmospheric pressure. The results are summarized in Table 1. The iron content of the supported iron catalysts is also summarized in Table S1. Among the catalysts prepared from POMs with different numbers of iron nuclei, **Fe1**/SiO_2 and **Fe2**/SiO_2 exhibited relatively high HCHO yields of 0.73% and 0.57%, respectively (Table 1, Entries 1, 9, and 10). **Fe4**/SiO_2 exhibited a relatively high CH_4 conversion of 3% but a low HCHO selectivity of 11%, resulting in a low HCHO yield of 0.33%. 35 wt% **Fe2**/SiO_2 (35**Fe2**/SiO_2) was prepared using **Fe2** with the same iron loading amount as that of **Fe4**/SiO_2, and the reaction was performed using 35**Fe2**/SiO_2. As a result, 35**Fe2**/SiO_2 exhibited lower CO_2 selectivity than **Fe4**/SiO_2 (Table 1, Entries 10 and 11). In addition, Cs-**Fe2**/SiO_2 was prepared to improve the thermal stability of the anionic structure of **Fe2**,[46] and the CH_4 oxidation performance of Cs-**Fe2**/SiO_2 was investigated under the same reaction conditions. However, despite its high selectivity toward HCHO (73%), Cs-**Fe2**/SiO_2 exhibited relatively low CH_4 conversion (0.67%) (Table 1, Entry 12).

To investigate the structural differences between **Fe2**/SiO_2, 35**Fe2**/SiO_2 and **Fe4**/SiO_2 after the reaction, Fe K-edge XAFS measurements were performed, with the XANES and EXAFS spectra displayed in Figs. S4 and S5, respectively. The Fe K-edge XANES results indicated that the valence of Fe in each catalyst prepared from **Fe2** and **Fe4** was not different. In a previous study, **Fe2**/SiO_2 was directly used for the reaction without any

Table 2 Catalytic performance over supported **Fe2** catalysts on various supports[a]

Entry	Support	BET surface area [m^2 g^{-1}]	Conv. [%]	Sel. [%]			Yield [%]
			CH_4	HCHO	CO	CO_2	HCHO
1	SiO_2-Q50	67	0.71	57	35	8	0.41
2	SiO_2-Q30	100	0.96	43	44	13	0.42
3	SiO_2	278	1.4	41	45	14	0.57
4	SiO_2-Q6	386	2.0	36	46	18	0.73
5	Al_2O_3	158	6.1	–	82	18	–
6	ZrO_2	40	3.3	–	78	22	–
7	CeO_2	43	6.8	–	65	35	–
8	CeO_2[b]	43	0.79	–	69	31	–
9	Nb_2O_5	145	0.84	39	51	10	0.33
10	TiO_2	72	1.2	7	64	29	0.08
11	BN	6	0.28	57	24	19	0.16
12	HAP	9	0.12	67	n.d.	33	0.08

[a]Reaction conditions: supported **Fe2** catalyst (100 mg), CH_4:O_2:Ar = 2:1:7, 50 mL min^{-1}, 1 atm, 600 °C. [b]500 °C.

pretreatment.[45] In contrast, **Fe2**/SiO_2 in this study was used after calcination. The results of Fe K-edge XANES and EXAFS suggested that **Fe2**/SiO_2 prepared by calcination under air atmosphere formed a structure similar to that of **Fe2**/SiO_2 treated by the reaction gas (Fig. S4a and Fig. S5a,b).[45] In our previous report on **Fe2**/SiO_2 (used for CH_4 oxidation without precalcination),[45] it was revealed that **Fe2** was decomposed into FeO_x subnanoclusters (<1 nm) and WO_x nanoclusters (approximately 3 nm) on SiO_2 under CH_4 oxidation conditions at 600°C. Various control experiments and characterizations also revealed that the FeO_x subnanoclusters were the active species. Furthermore, the FeO_x subnanoclusters were dispersed on the WO_x nanoclusters, and as a result, excessive aggregation and deactivation of the effective FeO_x subnanoclusters were suppressed. Thus, a similar structure was expected to form over **Fe4**/SiO_2. The Fe K-edge XANES spectra of 35**Fe2**/SiO_2 and **Fe4**/SiO_2 suggested that they also had similar structures to the previously reported **Fe2**/SiO_2 (Fig. S4b).[45] On the other hand, we found that the peak intensity corresponding to the Fe–O bond in the first coordination sphere for **Fe2**/SiO_2 and 35**Fe2**/SiO_2 was higher than that for **Fe4**/SiO_2 in the Fe K-edge EXAFS spectra (Fig. S5c,d). This may be due to the larger number of WO_x nanoclusters near the FeO_x subnanoclusters in **Fe2**/SiO_2 and 35**Fe2**/SiO_2 than that in **Fe4**/SiO_2 since the amount of tungsten per iron in **Fe2** was larger than that in **Fe4**. Furthermore, in the Raman spectrum of **Fe2**/SiO_2, three main vibrational peaks were observed, corresponding to ν(W=O) at 980–960 cm^{-1}, ν(W–O_a–W) at 840–780 cm^{-1}, and ν(W–O_b–W) at 720–680 cm^{-1} (Fig. S6).[59,60] The terminal oxo species (W=O) corresponds to an isolated tungsten species. In contrast, in the spectrum of **Fe4**/SiO_2, two peaks corresponding to ν(W–O_a–W) and ν(W–O_b–W) were observed and no ν(W=O) peak was observed. Considering that **Fe2**/SiO_2 and **Fe4**/SiO_2 contained almost the same amount of tungsten, 5.3 wt% and 4.5 wt%, respectively, there was a sufficient amount of WO_x species near the FeO_x subnanoclusters. The remaining WO_x species on **Fe2**/SiO_2 formed the isolated tungsten species, possibly because the amount of tungsten per iron of **Fe2** was larger than that of **Fe4**. Thus, these results were consistent with the EXAFS spectra (Fig. S5). Therefore, the difference in the iron oxide subnanocluster structures formed on SiO_2 was reflected in the catalytic performance. In addition, 35**Fe2**/SiO_2 exhibited higher HCHO selectivity than **Fe4**/SiO_2, possibly due to the higher tungsten content and the presence of a larger number of tungsten oxide clusters, which inhibited the aggregation of FeO_x subnanoclusters. In summary, the iron oxide subnanocluster catalysts prepared from **Fe1** and **Fe2** exhibited the highest HCHO yield in CH_4 oxidation.

Support effect

The catalytic performance for CH_4 oxidation was investigated for **Fe2**-based catalysts prepared using various supports at 600 °C under atmospheric pressure. The results and specific surface areas of supported are summarized in Table 2. The results indicated that higher specific surface areas of SiO_2 supports resulted in higher CH_4 conversion (Table 2, Entries 1–4). This suggested that a higher dispersion state of the **Fe2** precursor on SiO_2 led to the generation of more dispersed iron oxide nanoclusters, resulting in increased CH_4 conversion and HCHO yield. The supported **Fe2** catalyst prepared using SiO_2-Q6, which had a very high specific surface area of 386 m^2 g^{-1}, exhibited the highest CH_4 conversion and HCHO yield of 2.0% and 0.73%, respectively. In contrast, despite having lower specific surface areas than SiO_2, the supported **Fe2** catalysts prepared using Al_2O_3, ZrO_2, and CeO_2 exhibited higher CH_4 conversion, resulting in the production of only CO_x (Table 2, Entries 5–7). In addition, the reaction was performed at 500 °C with **Fe2**/CeO_2, but the selectivity to HCHO did not increase, although the CH_4 conversion decreased (Table 2, Entry 8). Similar catalytic performance has been reported for $FePO_4$ catalysts supported on Al_2O_3, SiO_2, TiO_2, and ZrO_2, suggesting that the choice of support affects the overoxidation of HCHO.[18]

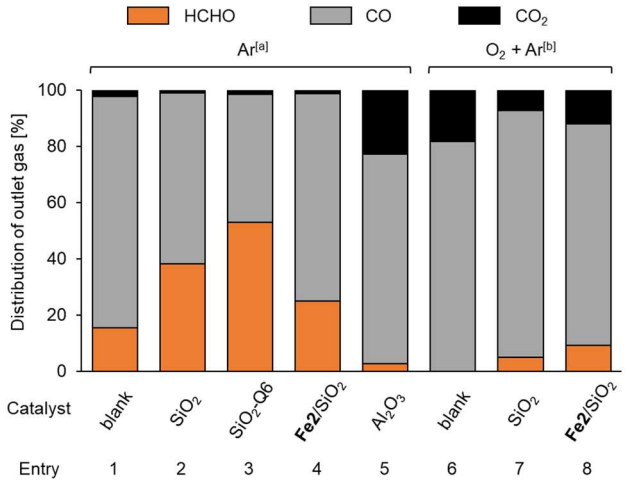

Fig. 2 HCHO pyrolysis and oxidation tests on various supports and **Fe2**/SiO_2. Reaction conditions: catalyst (100 mg), HCHO (1%), 1 atm, 600 °C. [a] Ar (50 mL min^{-1}), [b] O_2 (5 mL min^{-1}), Ar (45 mL min^{-1}).

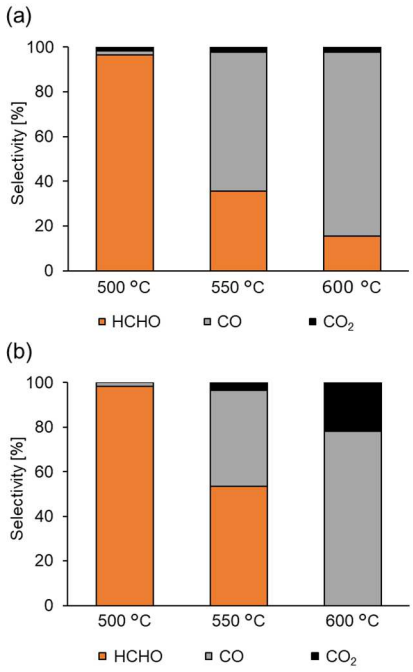

Fig. 3 Pyrolysis and oxidation tests without catalysts at various temperatures. Reaction conditions: no catalyst, 1 atm, HCHO (ca. 0.6%), (a) Ar (50 mL min^{-1}), (b) O_2 (5 mL min^{-1}), Ar (45 mL min^{-1}).

The surface acidity of these supports may promote the easy activation of CH_4, resulting in overoxidation of the products.[61] In addition, HAP, BN, Nb_2O_5, and TiO_2 had smaller specific surface areas than SiO_2, resulting in lower CH_4 conversion when used as supports for **Fe2** catalysts (Table 2, Entries 9–12). Therefore, the effect of the support on CH_4 oxidation was found to depend on the type of support and its specific surface area. Moreover, it was found that the **Fe2** catalyst supported on SiO_2, which was inert and had a high specific surface area, exhibited the highest HCHO yield.

Pyrolysis and oxidation tests of HCHO

As the support significantly affected the overoxidation of HCHO, pyrolysis and oxidation tests of HCHO on various supports and **Fe2**/SiO_2 were investigated (Fig. 2). The results indicated that HCHO was decomposed by 80% or more even in the absence of catalysts at 600 °C (Fig. 2, entry 1). We found that HCHO pyrolysis was significantly suppressed in the presence of SiO_2 (Fig. 2, entry 2), and this suppression increased with the specific surface area of SiO_2 (Fig. 2, entry 3). Additionally, HCHO pyrolysis was suppressed by using **Fe2**/SiO_2 (Fig. 2, entry 4). In contrast, HCHO pyrolysis on Al_2O_3 was promoted (Fig. 2, entry 5). HCHO overoxidation on SiO_2 was more suppressed even in the presence of O_2 than in the absence of catalysts (Fig. 2, entries 6 and 7). Furthermore, HCHO conversion using **Fe2**/SiO_2 was lower than that in the absence of catalysts (Fig. 2, entry 8). These findings suggested that the reason for the high HCHO yield when using **Fe2**/SiO_2 was the suppression of HCHO pyrolysis by SiO_2 and the use of **Fe2** as a catalyst precursor. Meanwhile, even with an inert support such as SiO_2, HCHO was sequentially oxidized in the presence of O_2 at 600 °C. Since a significant amount of HCHO was thermally decomposed even at 600 °C, pyrolysis and oxidation tests without catalysts were conducted at various temperatures, as illustrated in Fig. 3. The results indicated that both pyrolysis and oxidation were suppressed at lower temperatures and that almost no pyrolysis or oxidation occurred at 500 °C. In our previous study, however, the CH_4 conversion over **Fe2**/SiO_2 at 550 °C was lower than 1%, and the CH_4 conversion at 500 ℃ predicted based on the Arrhenius plots was below 0.4%.[45] Therefore, FeO_x subnanocluster active site should be modified and improved to archive higher HCHO yield at 500 °C.

Proposed mechanism of the suppression of HCHO pyrolysis

To elucidate the mechanism by which pyrolysis of HCHO was promoted on Al_2O_3 and suppressed on SiO_2, *in situ* DRIFTS measurements were conducted at 600 °C. The DRIFTS spectra measured 60 min after evacuation following HCHO flow were presented in Fig.4. The observed peaks of DRIFTS spectra and their assignments are summarized in Table S2[62–64]. Furthermore, time variation of *in situ* DRIFTS spectra of Al_2O_3 and SiO_2 at 600 °C is illustrated in Fig. S7. In the spectrum of Al_2O_3, three peaks observed at 1572, 2906, and 2997 cm^{-1} were attributed to formate species (Fig. 4a). In addition, the peaks at 1630 and 3751 cm^{-1} were attributed to H_2O and an aluminol group, respectively, indicating that these species possibly involved in the mechanism.

On the other hand, in the spectrum of SiO_2, two sharp peaks at 2959 and 2858 cm^{-1} were observed (Fig. 4b). From the previously reported data summarized in Table. S2, these peaks can be attributed to dioxymethylene species. As well as Al_2O_3, the peaks derived from adsorbed H_2O[65] at 3540 cm^{-1} and a silanol group[66] at 3736 cm^{-1} were observed. These findings suggested that the adsorbed HCHO was decomposed into formate on Al_2O_3, while not on SiO_2.

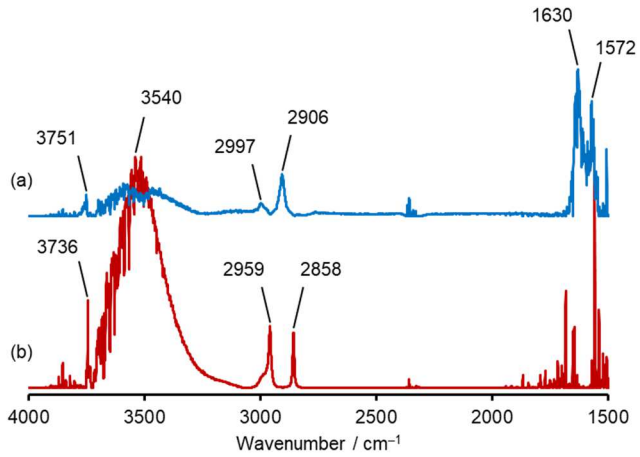

Fig. 4 *In situ* DRIFTS spectra on (a) Al_2O_3 and (b) SiO_2. Analysis conditions: HCHO/N_2 mixture gas (20 mL min^{-1}) flowed at 600 °C for 60 min. Then, the cell was evacuated, and DRIFTS spectra were measured 60 min later. The absorbance intensity on the vertical axis was Kubelka–Munk-transformed.

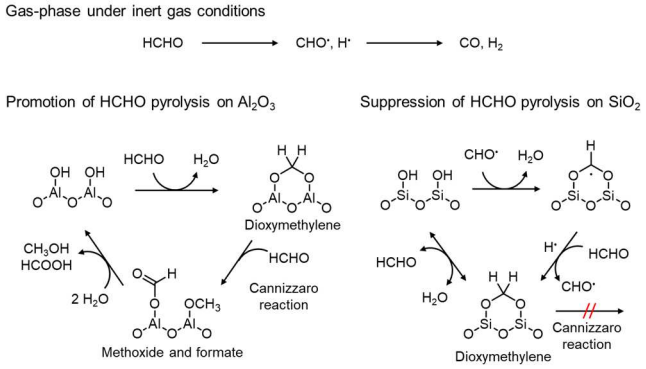

Fig. 5 Proposed mechanism of the suppression of HCHO pyrolysis on SiO_2 and the promotion of HCHO pyrolysis on Al_2O_3.

We proposed a surface reaction mechanism of HCHO on Al_2O_3 and SiO_2 based on the results of *in situ* DRIFTS, as displayed in Fig. 5. In the gas phase, CO is generated by HCHO pyrolysis via the formyl radical.[67] In the presence of Al_2O_3, HCHO reacts with aluminol groups on the surface to form dioxymethylene species. Then, the dioxymethylene species reacts with another HCHO to afford formate and methoxide species via the Cannizzaro reaction.[62] Then, these species further react with H_2O to form formic acid and methanol; however, due to the high temperature of 600 °C, they are possibly sequentially oxidized to CO_x. Therefore, Al_2O_3 undesirably promotes the overoxidation of HCHO to CO_x.

In contrast, the dioxymethylene species adsorbed on SiO_2 do not cause the Cannizzaro reaction because SiO_2 possesses no strong acidic or basic sites. Moreover, the formyl radical reacts with silanol species, and adsorbed on SiO_2. Then, the adsorbed radical species reacts with hydrogen atom or accepts hydrogen atom from HCHO to form dioxymethylene. Since the adsorbed dioxymethylene species reacts with H_2O to generate HCHO, we consider that HCHO pyrolysis can be suppressed on SiO_2. SiO_2-Q6 suppressed HCHO pyrolysis more than SiO_2 possibly because SiO_2-Q6 possessed more silanol groups to react with formyl radicals due to higher specific surface area.

Conclusions

The catalytic performance for CH_4 oxidation using SiO_2-supported metal oxide subnanocluster catalysts prepared from various POM precursors indicated that **Fe1**/SiO_2 and **Fe2**/SiO_2 exhibited the highest HCHO yields among oxide subnanocluster catalysts with 3d metal or Ce metal multinuclear oxide cores. In addition, we found that **Fe2**-based catalysts prepared using SiO_2 with a high specific surface area improved both the CH_4 conversion and HCHO yield. Pyrolysis and oxidation tests of HCHO on various supports revealed that HCHO was almost completely decomposed even in the absence of catalysts at 600 °C. Moreover, the pyrolysis and overoxidation of HCHO were suppressed when SiO_2 was used as the support. *In situ* DRIFTS measurement under HCHO flow demonstrated that the pyrolysis and oxidation of HCHO were suppressed on SiO_2, while the pyrolysis of HCHO was promoted on Al_2O_3. Thus, to achieve even higher HCHO yields in the future, it is necessary to suppress the pyrolysis and oxidation of HCHO in the gas phase. As pyrolysis and oxidation did not occur below 500 °C in the absence of catalysts, it is necessary to develop more effective catalysts that can lower the temperature of CH_4 activation.

Conflicts of interest

There are no conflicts to declare.

Acknowledgements

This work was financially supported by JSPS KAKENHI Grant Number 22K14539, 22H04971 and JST CREST Grant Number JPMJCR17P4. We greatly appreciate Dr. Hironori Ofuchi (Japan Synchrotron Radiation Research Institute, SPring-8) for the support of XAFS measurements at BL14B2, Proposal Number 2022B1656 and 2023A1512.

Notes and references

1 D. Sutton, B. Kelleher and J. R. H. Ross, *Fuel Process. Technol.*, 2001, **73**, 155–173.
2 J. Kopyscinski, T. J. Schildhauer and S. M. A. Biollaz, *Fuel*, 2010, **89**, 1763–1783.
3 G. Strobel, B. Hagemann, T. M. Huppertz and L. Ganzer, *Renewable Sustainable Energy Rev.*, 2020, **123**, 109747.
4 J. Kondori, S. Zendehboudi and L. James, *Fuel*, 2019, **249**, 264–276.
5 F. M. Mota and D. H. Kim, *Chem. Soc. Rev.*, 2019, **48**, 205–259.
6 M. Held, D. Schollenberger, S. Sauerschell, S. Bajohr and T. Kolb, *Chemie Ingenieur Technik*, 2020, **92**, 595–602.
7 A. Giocoli, V. Motola, N. Scarlat, N. Pierro and S. Dipinto, *Renewable Sustainable Energy Transition*, 2023, **3**, 100051.
8 M. C. Alvarez-Galvan, N. Mota, M. Ojeda, S. Rojas, R. M. Navarro and J. L. G. Fierro, *Catal. Today*, 2011, **171**, 15–23.
9 C. Hammond, S. Conrad and I. Hermans, *ChemSusChem*, 2012, **5**, 1668–1686.

10 P. Schwach, X. Pan and X. Bao, *Chem Rev.*, 2017, **117**, 8497−8520.
11 N. F. Dummer, D. J. Willock, Q. He, M. J. Howard, R. J. Lewis, G. Qi, S. H. Taylor, J. Xu, D. Bethell, C. J. Kiely and G. J. Hutchings, *Chem. Rev.*, 2023, **123**, 6359–6411.
12 T. J. Hall, J. S. J. Hargreaves, G. J. Hutchings, R. W. Joyner and S. H. Taylor, *Fuel Process. Technol.*, 1995, **42**, 151–178.
13 J. H. Lunsford, *Catal. Today*, 2000, **63**, 165–174.
14 K. Otsuka and M. Hatano, *J. Catal.*, 1987, **108**, 252–255.
15 E. M. Coda, E. Mulhall, R. van Hoek and B. K. Hodnett, *Catal. Today*, 1989, **4**, 383–387.
16 A. Parmaliana and F. Arena, *J. Catal.*, 1997, **167**, 57–65.
17 K. Aoki, M. Ohmae, T. Nanba, K. Takeishi, N. Azuma, A. Ueno, H. Ohfune, H. Hayashi and Y. Udagawa, *Catal. Today*, 1998, **45**, 29–33.
18 R. L. McCormick and G. O. Alptekin, *Catal. Today*, 2000, **55**, 269–280.
19 N. Ohler and A. T. Bell, *J. Phys. Chem. B*, 2006, **110**, 2700–2709.
20 A. de Lucas, J. L Valverde, L. Rodriguez, P. Sanchez and M. T. Garcia, *Appl. Catal. A*, 2000, **203**, 81–90.
21 N. V. Beznis, A. N. C. van Laak, B. M. Weckhuysen and J. H. Bitter, *Micropor. Mesopor. Mater.*, 2011, **138**, 176–183.
22 T. Akiyama, R. Sei and S. Takenaka, *Catal. Sci. Technol.*, 2021, **11**, 5273–5281.
23 S. Pei, B. Yue, L. Qian, S. Yan, J. Cheng, Y. Zhou, S. Xie and H. He, *Appl. Catal. A*, 2007, **329**, 148–155.
24 A. Matsuda, H. Tateno, K. Kamata and M. Hara, *Catal. Sci. Technol.*, 2021, **11**, 6987–6998.
25 T. Akiyama, M. Shimakawa and S. Takenaka, *Chem. Lett.*, 2022, **51**, 511–514.
26 A. de Lucas, J. L. Valverde, P. Cañizares and L. Rodriguez, *Appl. Catal. A*, 1999, **184**, 143–152.
27 Q. Zhang, W. Yang, X. Wang, Y. Wang, T. Shishido, and K. Takehira, *Micropor. Mesopor. Mater.*, 2005, **77**, 223–234.
28 F. Arena, G. Gatti, G. Martra, S. Coluccia, L. Stievano, L. Spadaro, P. Famulari, A. Parmaliana, *J. Catal.*, 2005, **231**, 365–380.
29 Y. Li, D. An, Q. Zhang, and Y. Wang, *J. Phys. Chem. C*, 2008, **112**, 13700–13708.
30 Q. Zhang, Y. Li, D. An and Y. Wang, *Appl. Catal. A*, 2009, **356**, 103–111.
31 J. He, Y. Li, D. An, Q. Zhang and Y. Wang, *J. Nat. Gas Chem.*, 2009, **18**, 288–294.
32 Y. Kim, T. Y. Kim, C. K. Song, K. R. Lee, S. Bae, H. Park, D. Yun, Y. S. Yun, I. Nam, J. Park, H. Lee and J. Yi, *Nano Energy*, 2021, **82**, 105704.
33 H. Berndt, A. Martin, A. Brückner, E. Schreier, D. Müller, H. Kosslick, G.-U. Wolf, and B. Lücke, *J. Catal.*, 2000, **191**, 384–400.
34 T. Kobayashi, N. Guilhaume, J. Miki, N. Kitamura, and M. Haruta, *Catal. Today*, 1996, **32**, 171–175.
35 M. Sun, J. Zhang, P. Putaj, V. Caps, F. Lefebvre, J. Pelletier and J.-M. Basset, *Chem. Rev.*, 2014, **114**, 981–1019.
36 S.-S. Wang and G.-Y. Yang, *Chem. Rev.*, 2015, **115**, 4893–4962.
37 P. Putaj and F. Lefebvre, *Coord. Chem. Rev.*, 2011, **255**, 1642–1685.
38 D.-L. Long, R. Tsunashima and L. Cronin, *Angew. Chem. Int. Ed.*, 2010, **49**, 1736–1758.
39 A. Tézé, G. Hervé, R. G. Finke and D. K. Lyon, *Inorg. Synth.*, 1990, **27**, 85–96.
40 K. Suzuki, M. Shinoe and N. Mizuno, *Inorg. Chem.*, 2012, **51**, 11574–11581.
41 K. Suzuki, F. Tang, Y. Kikukawa, K. Yamaguchi and N. Mizuno, *Angew. Chem. Int. Ed.*, 2014, **53**, 5356–5360.
42 K. Suzuki, R. Sato, T. Minato, M. Shinoe, K. Yamaguchi and N. Mizuno, *Dalton Trans.*, 2015, **44**, 14220–14226.
43 Y. Sunada, K. Yamaguchi and K. Suzuki, *Coord. Chem. Rev.*, 2022, **469**, 214673.
44 Y. Koizumi, K. Yonesato, K. Yamaguchi and K. Suzuki, *Inorg. Chem.*, 2022, **61**, 9841–9848.
45 K. Wachi, T. Yabe, T. Suzuki, K. Yonesato, K. Suzuki and K. Yamaguchi, *Appl. Catal. B*, 2022, **314**, 121420.
46 T. Suzuki, T. Yabe, K. Wachi, K. Yonesato, K. Suzuki and K. Yamaguchi, *ChemNanoMat*, 2023, **9**, e202200428.
47 A. K. Pandey, T. Gupta, and B. P. Baranwal, *Transition Met. Chem.*, 2004, **29**, 370–375.
48 T. Minato, K. Suzuki, K. Kamata and N. Mizuno, *Chem. Eur. J.*, 2014, **20**, 5946–5952.
49 T. Minato, K. Suzuki, K. Yamaguchi and N. Mizuno, *Chem. Eur. J.*, 2017, **23**, 14213–14220.
50 E. Takahashi, K. Kamata, Y. Kikukawa, S. Sato, K. Suzuki, K. Yamaguchi and N. Mizuno, *Catal. Sci. Technol.*, 2015, **5**, 4778–4789.
51 N. Nakagawa, K. Uehara and N. Mizuno, *Inorg. Chem.*, 2005, **44**, 9068–9075.
52 K. Nomiya, K. Yagishita, Y. Nemoto and T. Kamataki, *J. Mol. Catal. A*, 1997, **126**, 43–53.
53 Y. Kuriyama, Y. Kikukawa, K. Suzuki, K. Yamaguchi and N. Mizuno, *Chem. Eur. J.*, 2016, **22**, 3962–3966.
54 M. S. Balula, J. A. Gamelas, H. M. Carapuça, A. M. V. Cavaleiro and W. Schlindwein, *Eur. J. Inorg. Chem.*, 2004, **2004**, 619–628.
55 F. Zonnevijlle, C. M. Tourne, and G. F. Tourne, *Inorg. Chem.*, 1982, **21**, 2751–2757.
56 R. Al-Oweini, B. S. Bassil, J. Friedl, V. Kottisch, M. Ibrahim, M. Asano, B. Keita, G. Novitchi, Y. Lan, A. Powell, U. Stimming and U. Kortz, *Inorg. Chem.*, 2014, **53**, 5663–5673.
57 Y.-F. Han, L. Chen, K. Ramesh, Z. Zhong, F. Chen, J. Chin and H. Mook, *Catal. Today*, 2008, **131**, 35–41.
58 H. Wang, C. Chen, Y. Zhang, L. Peng, S. Ma, T. Yang, H. Guo, Z. Zhang, D. S. Su and J. Zhang, *Nat. Commun.*, 2015, **6**, 7181.
59 E. I. Ross-Medgaarden and I. E. Wachs, *J. Phys. Chem. C*, 2007, **11**, 15089–15099.
60 S. Chen, L. Zeng, H. Tian, X. Li and J. Gong, *ACS Catal.*, 2017, **7**, 3548–3559.
61 W. H. Cheng, *J. Catal.*, 1996, **158**, 477–485.
62 G. Busca, J. Lamotte, J.-C. Lavalley and V. Lorenzelli, *J. Am. Chem. Soc.*, 1987, **109**, 5197–5202.
63 D. B. Clarke, D. K. Lee, M. J. Sandoval and A. T. Bell, *J. Catal.*, 1994, **150**, 81–93.
64 S. Kattel, B. Yan, Y. Yang, J. G. Chen and P. Liu, *J. Am. Chem. Soc.*, 2016, **138**, 12440–12450.
65 D. B. Clarke and A. T. Bell, *J. Catal.*, 1995, **154**, 314–328.
66 M. A. Bañares, L. J. Alemany, M. López Granados, M. Faraldos and J. L. G. Fierro, *Catal. Today*, 1997, **33**, 73–83.
67 R. Klein, M.D. Scheer and L. J. Schoen, *J. Am. Chem. Soc.*, 1956, **78**, 50–52

